Available online at www.sciencedirect.com

ScienceDirect

Journal of Nuclear Materials 362 (2007) 75–86

journal of nuclear materials

www.elsevier.com/locate/jnucmat

Characterization of hot deformation behavior of Zr–1Nb–1Sn alloy

J.K. Chakravartty [a,*], R. Kapoor [a], S. Banerjee [b], Y.V.R.K. Prasad [c]

[a] Materials Science Division, Bhabha Atomic Research Centre, Mumbai 400 085, India
[b] Materials Group, Bhabha Atomic Research Centre, Mumbai 400 085, India
[c] Department of Metallurgy, Indian Institute of Science, Bangalore 560 012, India

Received 7 August 2006; accepted 14 November 2006

Abstract

The hot deformation behavior of β-quenched Zr–1Nb–1Sn was studied in the temperature range 650–1050 °C and strain rate range 0.001–100 s^{-1} using processing maps. These maps revealed three different domains: a domain of dynamic recovery at temperatures <700 °C and at strain rates $<3\times10^{-3}\ s^{-1}$, a domain of dynamic recrystallization in the temperature range 750–950 °C and at strain rates $<10^{-2}\ s^{-1}$ with a peak at 910 °C and $10^{-3}\ s^{-1}$ (in $\alpha+\beta$ phase field), and a domain of large-grain superplasticity in the β phase field at strain rates $<10^{-2}\ s^{-1}$. In order to identify the rate controlling mechanisms involved in these domains, kinetic analysis was carried out to determine the various activation parameters. In addition, the processing maps showed a regime of flow instability spanning both $\alpha+\beta$ and β phase fields. The hot deformation behavior of Zr–1Nb–1Sn was compared with that of Zr, Zr–2.5Nb and Zircaloy-2 to bring out the effects of alloy additions.

1. Introduction

The drive towards improved thermal efficiencies of nuclear reactor systems requires the use of fuels with higher burn up, higher coolant temperature and partial boiling of coolant. The first generation fuel tube materials like Zircaloys and binary Zr–Nb alloys have been found unsuitable under the operational conditions because of irradiation enhanced corrosion, creep and growth, the irradiation induced water side corrosion being the life limiting factor of fuel tubes [1,2]. This has led to the development of new zirconium alloys to meet the challenges demanded by the enhanced fuel performance. The resistance to long term corrosion, lower irradiation induced growth and creep, and adequate mechanical properties are some important considerations. In this respect, quaternary Zr–Nb–Sn–Fe alloys, have shown considerable promise [1–4]. Under pressurized water reactor (PWR) operating conditions, quaternary Zr–Nb–Sn–Fe alloys perform better than both Zircaloys and binary Zr–Nb in terms of in-pile corrosion, creep and growth [1–4]. While in-pile corrosion in these alloys is

---

[*] Corresponding author. Tel.: +91 22 25593816; fax: +91 22 25515151.
E-mail address: jayanta@barc.ernet.in (J.K. Chakravartty).

0022-3115/$ - see front matter © 2006 Elsevier B.V. All rights reserved.
doi:10.1016/j.jnucmat.2006.11.007

controlled primarily by the microstructure with strong dependence on the precipitate type, size and distribution, the crystallographic texture has strong influence on hydride orientation, stress corrosion cracking and irradiation creep. It is known that in addition to chemistry of the alloy, both microstructure and texture are important in mitigating the life limiting factors of in-core zirconium components.

The hot working parameters such as temperature and strain rate affect not only the microstructure of the product (in fact the scale of microstructure and basic texture of the finished tube is determined at this stage) but also its capacity to undergo subsequent cold working operations. While the microstructure–property correlations in these alloys have been established in relation to in-reactor behavior by several investigators [1–4], limited information is available on the mechanisms of hot deformation. Further, zirconium alloys, like titanium alloys, are prone to flow instabilities during deformation at moderate rates which in turn are known to cause local changes in microstructure.

Several processes such as recovery, recrystallization and superplasticity, which occur dynamically during the hot deformation of zirconium alloys containing both α and β stabilizers have been identified earlier [5–10]. In these investigations it was found that the dynamic recrystallization (DRX) of α phase is the dominant high temperature process during deformation in both α and $\alpha+\beta$ phase fields. As regards the effect of alloying addition on the deformation characteristics, it has been observed that α stabilizers have virtually no effect on hot deformation behavior of the α phase while addition of β stabilizers like Nb alter the deformation characteristics dramatically [5,8,9]. For example, addition of 2.5 wt% Nb lowers the strain rate required for DRX by two orders of magnitude compared to that required for DRX of unalloyed Zr.

The aim of the present investigation is twofold: (i) to study the characteristics of hot deformation of Zr–1 wt%Nb–1 wt%Sn alloy over a wide range of temperatures and strain rates with a view to optimize its hot workability and to identify the high temperature processes that occur dynamically, and (ii) to compare hot deformation behavior of this alloy with that of commercially pure Zr, Zr–2.5Nb and Zircaloy-2 (primarily Zr–1.5Sn) for bringing out the combined effects of Sn (α stabilizer) and Nb (β stabilizer) additions.

In this investigation, the hot working characteristics are studied using the approach of processing maps in the format of dynamic materials model proposed by Gegel et al. [11] and reviewed recently by Prasad and Seshacharyulu [12]. The basis and principles of this approach have been described earlier and its applications to hot working of a wide range of alloys have been compiled [12,13]. Here the work piece is considered as a dissipator of power under hot working conditions and the total power at any instant is converted into two complementary forms: thermal and microstructural which are not recoverable by the system. The factor that partitions power between these two is the strain rate sensitivity of flow stress (m) which is unity for an ideal linear dissipator. The efficiency of power dissipation η of a non-linear dissipator is expressed as [12]

$$\eta = \frac{2m}{m+1}. \tag{1}$$

The variation of the efficiency of power dissipation plotted as a function of temperature (T) and strain rate ($\dot{\varepsilon}$) is known as power dissipation map and represents the pattern in which power is dissipated through microstructural changes. The three-dimensional variation is better viewed as an iso-efficiency contour map sectioned parallel to the $\dot{\varepsilon}$–T plane. Over this variation is superimposed a continuum instability criterion for identifying regimes of flow instabilities, developed on the basis of extremum principles of irreversible thermodynamics as applied to large plastic flow [14]. The criterion is given in the form of another non-dimensional parameter [12,15] called instability parameter ξ:

$$\xi = \frac{\partial \ln\left(\frac{m}{m+1}\right)}{\partial \ln \dot{\varepsilon}} + m. \tag{2}$$

Flow instabilities are predicted when $\xi < 0$ and must be avoided during processing. These two maps together constitute a processing map which exhibits domains within which specific microstructural mechanisms operate as well regimes where there will be flow instabilities like adiabatic shear band formation or flow localization. This method has been found very effective in delineating the range of strain rates and temperatures over which a specific mechanism dominates despite several metallurgical processes occurring simultaneously during hot deformation [6]. Another advantage of this approach is that prior knowledge or evaluation of the atomistic mechanisms is not required. This method has been used extensively to model hot deformation of several zirconium alloys [6].

2. Experimental

The alloy studied here was obtained from Nuclear Fuel Complex, Hyderabad, India, in the form of extruded and cold drawn rods with nominal composition (wt%) of Zr–1Sn–1Nb–0.1Fe–0.12O (henceforth referred to as Zr–Nb–Sn alloy). The $\alpha \rightarrow \alpha + \beta$ and $\alpha + \beta \rightarrow \beta$ transformation temperatures of this material as determined by a dilatometer were 710 °C and 960 °C, respectively. Prior to testing the specimens were heat treated at 1020 °C (in the β phase field) for 30 min in quartz tubes sealed under helium pressure and water quenched. The quenching resulted in an acicular morphology of α' martensite (transformed β) as shown in Fig. 1. On heating to various testing temperatures in the $\alpha + \beta$ range the volume fractions of both α and β phases change with temperature. Cylindrical specimens of 10 mm diameter and 15 mm height were machined such that the compression axis of the specimens was along the extrusion direction. A 0.8 mm diameter hole was drilled on the surface of the specimen for the insertion of a thermocouple. This thermocouple was also useful in measuring the adiabatic temperature rise during deformation. Hot compression tests were conducted in a matrix of nine temperatures in the range 650–1050 °C and six strain rates in the range 0.001–100 s^{-1}. To achieve a constant true strain rate during deformation, tests were performed on a computer-controlled servohydraulic machine. The temperature control was within ±2 °C and the adiabatic temperature rise during compression was measured with the help of a transient recorder. The specimens were coated with borosilicate glass powder which acted as lubricant as well as a protective cover of the specimen against oxidation at high temperatures. Concentric grooves of about 0.5 mm depth were engraved on the specimen faces to facilitate the retention of the glass lubricant. The specimens were compressed to about half their height and water quenched rapidly from the test temperature. The deformed specimens were sectioned parallel to the compression axis and metallographic investigations were carried out using standard techniques. The grain size was determined by linear intercept method. TEM specimens were prepared by jet polishing using a solution of methanol, perchloric acid and *n*-butanol at −40 °C. Tensile ductility of the material in the temperature range 650–1050 °C was measured on cylindrical specimens with 4 mm diameter and 25 mm gauge length and at a nominal strain rate of about 0.001 s^{-1} in a screw driven universal testing machine.

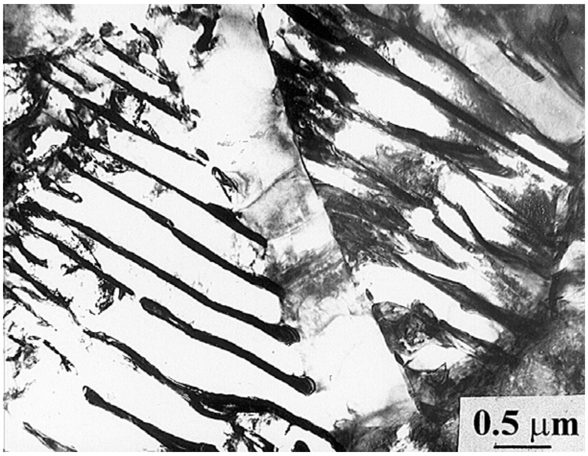

Fig. 1. TEM micrograph of Zr–Nb–Sn alloy on β-quenching. The plate type morphology of α' can be seen in transformed β microstructure.

The load–displacement data obtained from compression tests were processed to obtain true stress (σ) vs. true plastic strain (ε) curves using standard equations. The true plastic strain was obtained by subtracting the elastic strain components of specimen and load train of test machine from the total strain. The variation of σ with T and $\dot{\varepsilon}$ was obtained from the σ–ε curves. These data were corrected for the adiabatic temperature rise by using linear interpolation of $\log\sigma$ vs. $1/T$ plot. On the basis of the corrected flow stress data, the processing maps were developed using the following computational procedure: $\log\sigma$ vs. $\log\dot{\varepsilon}$ was fitted using a cubic spline function and the m was calculated as a function of $\dot{\varepsilon}$. This was repeated at different temperatures. The efficiency of power dissipation η was then calculated from a set of m values as a function of $\dot{\varepsilon}$ and T and plotted as an iso-efficiency contour map in the $\dot{\varepsilon}$–T plane.

3. Results and analysis

3.1. Flow stress behavior

The σ–ε curves at various strain rates corresponding to 800 and 1050 °C are shown in Fig. 2. These are representative of the deformation

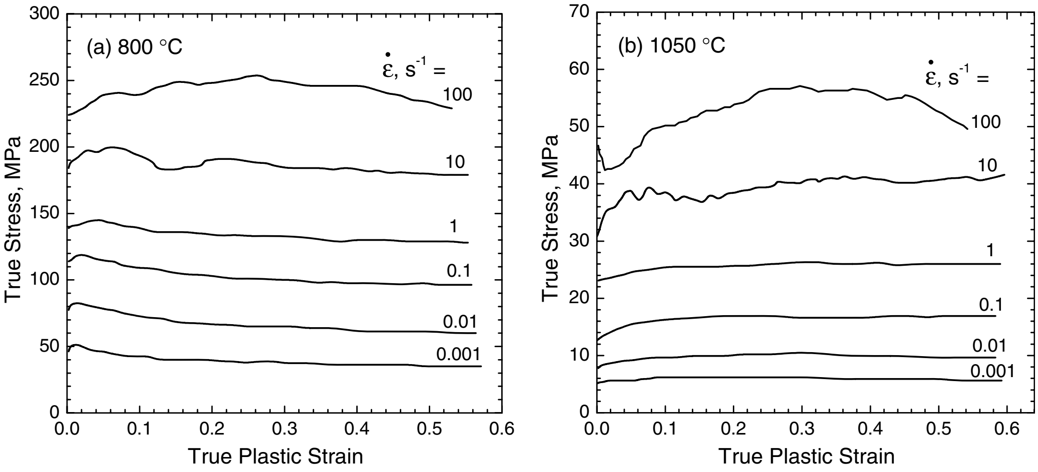

Fig. 2. Flow curves of Zr–Nb–Sn alloy deformed in compression at different strain rates for: (a) 800 °C in the $\alpha + \beta$ phase field, (b) 1050 °C in the β phase field.

behavior of the two phase $\alpha + \beta$ regime and the single phase β regime, respectively. At 800 °C in the $\alpha + \beta$ phase field and $\dot{\varepsilon} < 1\ \mathrm{s}^{-1}$, the flow curves exhibits continuous flow softening after a peak stress; the extent of softening decreases with increasing strain rate (Fig. 2(a)). This behavior is similar to that exhibited by many Ti and Zr alloys during deformation in the $\alpha + \beta$ phase field with a transformed β microstructure and this is considered to be a typical flow behavior [6,16,17]. It is well known that these flow curves tend to reach steady state at larger strains. In contrast to these, deformation in the β phase field shows a steady state flow behavior at $\dot{\varepsilon} < 1\ \mathrm{s}^{-1}$ as shown in Fig. 2(b). This behavior is again a characteristic feature of deformation in single phase β of zirconium and titanium alloys [7,18–20]. In the predominantly α phase (i.e. below $\alpha \rightarrow \alpha + \beta$ transformation temperature), the σ–ε curves up to 700 °C and $\dot{\varepsilon} < 1\ \mathrm{s}^{-1}$ exhibited flow softening after a peak stress followed by a steady state behavior at large strains (>0.5). At $\dot{\varepsilon} \geqslant 1\ \mathrm{s}^{-1}$ and at all temperatures of testing, oscillatory flow curves indicating inhomogeneous flow behavior were obtained. Similar oscillatory flow curves have also been reported in various Zr alloys at $\dot{\varepsilon} > 1\ \mathrm{s}^{-1}$ [5–10]. Table 1 gives the σ, $\dot{\varepsilon}$, T data at $\varepsilon = 0.5$. The σ values listed in the table have been corrected for adiabatic temperature rise for $\dot{\varepsilon} \geqslant 1\ \mathrm{s}^{-1}$.

Table 1
Flow stress values (MPa) of β-quenched Zr–Nb–Sn alloy at various strain rates and temperatures for a true strain of 0.5

Temperature (°C)	Strain rate (s^{-1})					
	10^{-3}	10^{-2}	10^{-1}	10^{0}	10^{1}	10^{2}
650	124.0	204.6	256.8	305.7	336.0	422.0
700	74.4	123.8	174.7	235.5	302.5	353.2
750	49.7	81.1	121.4	187.4	247.4	293.8
800	33.7	58.4	94.7	132.5	188.9	232.7
850	17.2	36.0	57.0	99.2	119.6	155.2
900	11.8	19.2	30.1	45.7	71.0	89.8
950	6.0	12.7	19.1	32.3	50.7	74.8
1000	6.5	11.1	18.8	28.4	45.1	54.4
1050	6	9.8	16.7	25.9	41.6	55.3

3.2. Power dissipation and instability maps

The processing map, obtained as described earlier, for the Zr–Nb–Sn alloy at $\varepsilon = 0.5$ is shown in Fig. 3. This reveals two domains: domain D_1 at low strain rates in the temperature range where the α phase is the dominant constituent, and domain D_2 encompassing almost the entire $\alpha + \beta$ range and a part of the β range (i.e. from 750 to 1010 °C), occurring at $\dot{\varepsilon} < 2 \times 10^{-2}\ \mathrm{s}^{-1}$. Here η reaches two local maxima, one with a peak of 40% occurring at 650 °C and 0.001 s^{-1} and other with a peak of 43% at 900 °C and 0.001 s^{-1}. This suggests that two different deformation mechanisms may be involved in these domains. However, it may also be noted that the domain D_2 closes at 1030 °C which is beyond $\alpha + \beta \rightarrow \beta$ transformation temperature of this material (960 °C). In this temperature range the alloy exists as $\alpha + \beta$ (volume fraction of each phase varying with temperature) below 960 °C, and a single phase β above this temperature. It is likely therefore that within the temperature

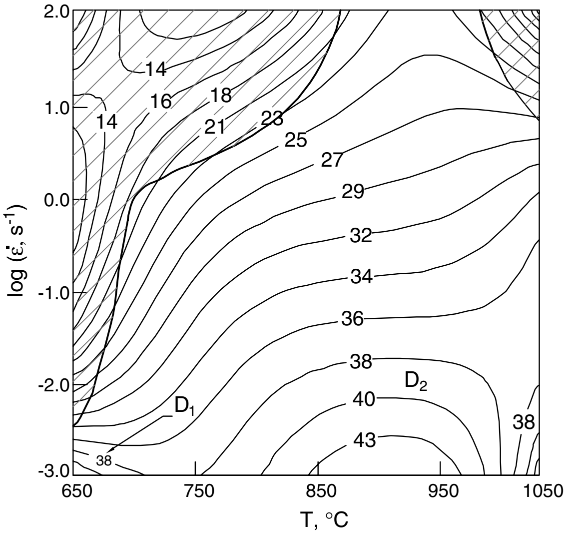

Fig. 3. Processing map of Zr–Nb–Sn alloy at a strain of 0.5 showing iso-efficiency contours and the instability regime. Contour numbers indicate efficiency of power dissipation in percent. Instability during processing occurs when the parameter $\xi < 0$ (refer Eq. (2)), and is shown here as the hatched areas.

bound of this domain the alloy may exhibit a variety of deformation mechanisms with similar power dissipation characteristics. The map shows a large regime of flow instability spanning both $\alpha + \beta$ and β phase fields. The first regime of instability for the alloy under investigation occurs within the temperature range 650–850 °C and $\dot{\varepsilon} > 0.01\ \mathrm{s}^{-1}$ and the other is located at upper right hand corner within the β phase field and at $\dot{\varepsilon} > 10\ \mathrm{s}^{-1}$. Since the σ–ε plots (Fig. 2) show that the material is in steady state at $\varepsilon = 0.5$, this map can be taken as representative; maps at other strains were not significantly different. In the following an attempt is made to identify the mechanisms occurring within the above domains on the basis of the microstructural features recorded on the deformed samples, observed variation of flow parameters and tensile ductility.

3.3. Deformed microstructure

The optical micrographs of the alloy deformed in the $\alpha + \beta$ phase field to $\varepsilon = 0.7$ are shown in Fig. 4(a)–(c). These reveal significant modification of the starting microstructure and exhibit equiaxed morphology of α phase separated by transformed β phase. It has been found that the α grain size varies with strain rate and temperature of deformation. However, α/β boundaries are not clearly visible under the etching conditions. A transmission electron micrograph of a specimen deformed at 750 °C and at $10^{-3}\ \mathrm{s}^{-1}$ is shown in Fig. 4(d). The microstructure is characterized by a morphology consisting of equiaxed α grains with β phases at the triple junction of α grains. This microstructure is representative of all the deformed structures within $\alpha + \beta$ phase field of the domain. When deformation is carried out predominantly in α phase (within domain D$_1$), it is seen that there is no major modification of the starting elongated morphology of α phase (Fig. 5(a)). In addition it is seen that there is a tendency for the formation of low angle boundaries presumably by accumulation of dislocation in low energy configurations (Fig. 5(b)). The features of deformation in the β phase field (samples deformed at temperatures >960 °C) could not be recorded because of its metastable nature. The microstructural features exhibited by the specimens deformed within the regime of flow instabilities in the $\alpha + \beta$ phase field are shown in Fig. 6. Seen here are flow localization bands wherein deformation appears confined. Similar flow localization and adiabatic shear bands have been reported in various Zr alloys [4–10]. The formation of these bands in Zr alloys is related to the adiabatic conditions prevailing at $\dot{\varepsilon} > 1\ \mathrm{s}^{-1}$ and its low thermal conductivity ($\sim$20 W m^{-1} K^{-1}). The instability features in the β regime (upper right hand corner of Fig. 3) could not be recorded as the microstructure of deformed samples was masked because of phase transformation during cooling subsequent to deformation.

3.4. Ductility measurement

The variation of tensile ductility (total elongation) as a function of testing temperature at a strain rate of $10^{-3}\ \mathrm{s}^{-1}$ is depicted in Fig. 7. Ductility increases with temperature with a peak ($\approx$250%) in the temperature range 850–950 °C where the processing map exhibits a peak efficiency of $\approx$43%. At temperatures higher than 960 °C (β transus) tensile ductility is lowered but maintains at reasonably high values (>120%). Similar ductility variation has been reported during hot deformation of Zr and Ti alloys [7,9,10,16,17].

3.5. Kinetic analysis

In order to identify the deformation mechanisms responsible for microstructural development during hot deformation, thermal activation analysis was

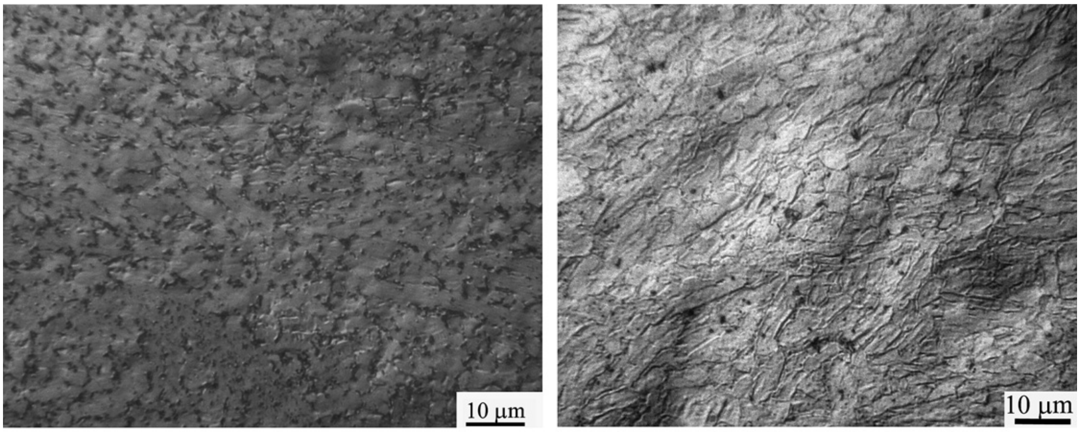

(a) 750°C (b) 850°C

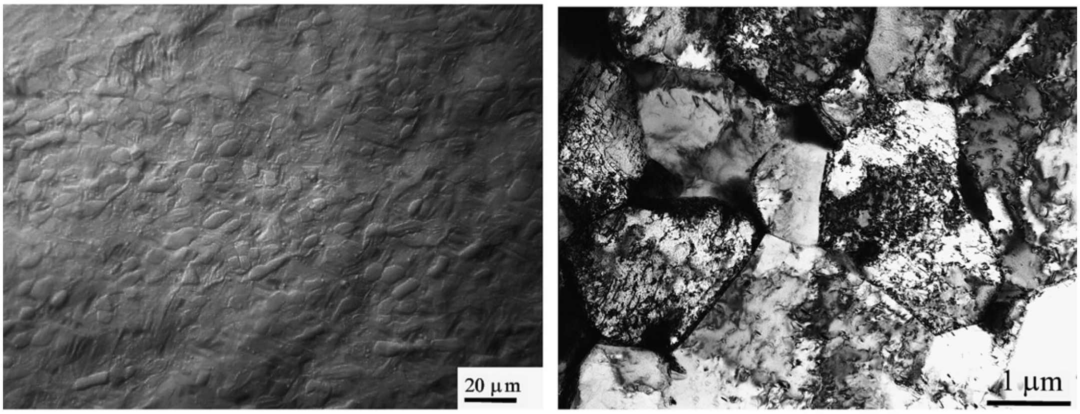

(c) 900°C (d) 750°C

Fig. 4. Microstructure of samples deformed to $\varepsilon = 0.7$ and at $\dot{\varepsilon} = 10^{-3}\ \mathrm{s}^{-1}$ and at various temperatures as indicated: (a–c) are optical micrographs showing equiaxed morphology of α grains, a change in α grain size with temperature is seen, and (d): TEM micrograph showing dislocation substructure within α grains and presence of β at the triple junction of grains.

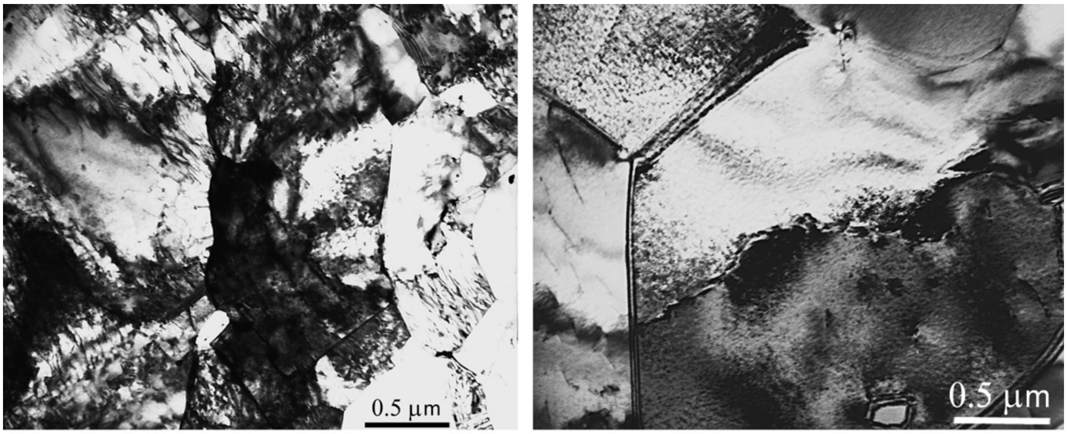

(a) 650°C 10^{-3} s^{-1} (b) 700°C 10^{-3} s^{-1}

Fig. 5. Typical TEM micrographs of samples deformed in the dynamic recovery domain showing, (a) the formation of substructure within starting elongated α grains, and (b) low angle sub-boundaries within the elongated α grains.

Fig. 6. Optical microstructure of samples deformed to $\varepsilon = 0.7$ at 700 °C and $10^1\ \mathrm{s}^{-1}$ in the unstable flow regime. Localized deformation bands are seen here. The compression axis is vertical.

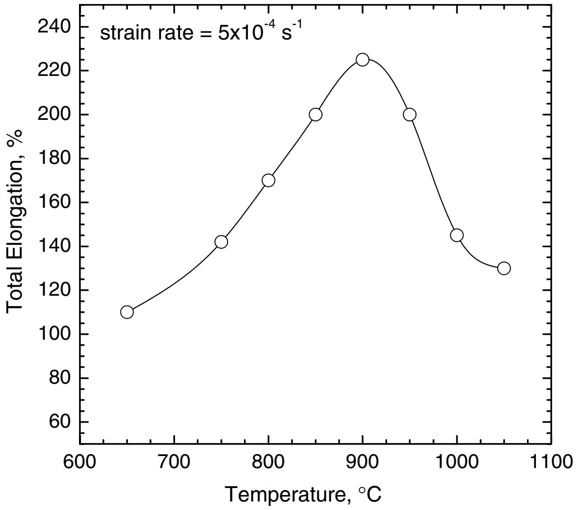

Fig. 7. The variation of tensile ductility (total elongation) as a function of testing temperature at a strain rate of $5 \times 10^{-4}\ \mathrm{s}^{-1}$.

carried out in the domain D_2. σ, $\dot{\varepsilon}$, T data from this domain were fitted to a kinetic rate equation of the form:

$$\dot{\varepsilon} = C\left(\frac{\sigma}{\mu}\right)^n \exp\left(\frac{-Q}{RT}\right), \tag{3}$$

where Q is the activation energy, n is the stress exponent, C is a constant, and μ is the shear modulus, taken as $\mu = 29.28 - 0.021T$ [21]. Although the domain extends beyond the β transus temperature of 960 °C the data used to fit Eq. (3) was taken up to 950 °C (corresponding to α + β phase field). Data in the β range was also fit to Eq. (3). The constants n, Q, and C were determined through the non-linear fitting of the data in both the α + β and β phase fields. The parameters were calculated to be $n = 3.8$ and $Q = 259$ kJ/mol in the α + β phase field, and $n = 4.24$, $Q = 110$ kJ/mol in the β phase field. The fit to Eq. (3) was checked by plotting temperature compensated strain rate Z vs. σ/μ on a log–log scale; where $Z = \dot{\varepsilon}\exp(Q/RT)$, the Zener–Hollomon parameter (Fig. 8). It is seen that for the parameters obtained the fit is good in both the α + β and β ranges.

The σ, $\dot{\varepsilon}$, and T data were analyzed by the standard method of thermally activated deformation using an expression of the form [22,23]

$$\dot{\varepsilon} = \dot{\varepsilon}_0 \exp(-\Delta G/RT), \quad \dot{\varepsilon}_0 = \phi b \rho_{\mathrm{m}} \lambda v, \tag{4a, b}$$

where ϕ is a scaling constant, b is the magnitude of Burgers vector, ρ_{m} is the mobile dislocation density, λ is the spacing between obstacles and v is the vibration frequency of the atoms. ΔG can in turn be expressed as a non-linear function of shear modulus corrected stress ($\sigma' = \sigma/\mu$) as [24,25]

$$\ln \dot{\varepsilon} = \ln \dot{\varepsilon}_0 - \frac{\Delta G_0}{RT}\left[1 - \left(\frac{\sigma'}{\sigma'_0}\right)^{0.5}\right]^{1.5}. \tag{5}$$

Here ΔG_0 represents the free energy required to overcome the barrier, σ'_0 ($=\sigma_0/\mu_0$) represents the strength of the barrier at 0 K. In the case of hot deformation it is likely that internal stresses do

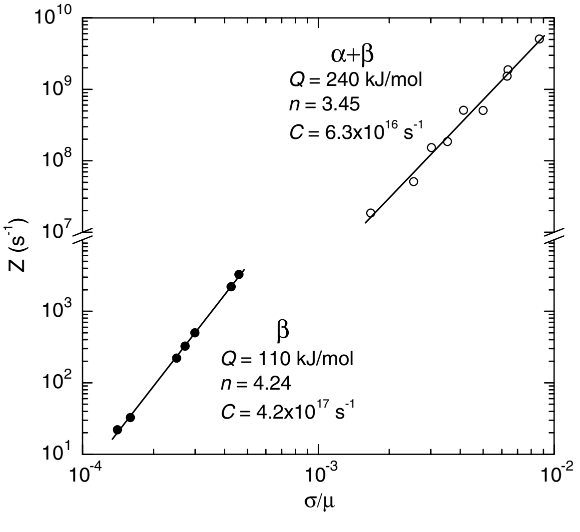

Fig. 8. Plot of Z vs. (σ/μ) in both the α + β and β phase field. This shows that the fit as per Eq. (3) is good. The values of fitted parameters n, Q, C, for each phase field are listed in the plot.

not play an important role and thus have been neglected in Eq. (5). The fitting was carried out with the data within the domains using non-linear regression analysis to obtain $\dot{\varepsilon}_0$, ΔG_0 and σ'_0. It can be seen from Eq. (5) that a plot of $(\sigma'/\sigma'_0)^{0.5}$ vs. $(RT/\Delta G_0 \ln(\dot{\varepsilon}_0/\dot{\varepsilon}))^{2/3}$ should yield a straight line. Fig. 9 shows the fit for parameters determined (as listed in the plot) for both α + β and β.

Activation volume is a thermodynamic parameter and can be physically thought of as a product of $A * b$ where A is the area associated with the movement of rate controlling species between short range obstacles and b is the magnitude of Burgers vector. Thermodynamically activation volume V is defined as $V = -\partial G/\partial\tau$. From Eq. (5) and using $\sigma = \mathrm{M}\tau$, where τ is shear stress and $M = 3$ is the Taylor factor, the experimental activation area A can be written as

$$A = \frac{3M\Delta G_0}{4\sigma_0 b}\left(1 - \left\{\frac{\sigma'}{\sigma'_0}\right\}^{0.5}\right)^{0.5}\left(\frac{\sigma'}{\sigma'_0}\right)^{-0.5}. \tag{6}$$

Fig. 10 shows a plot of A/b^2 vs. σ/μ for both the α + β phase and β phase fields. In the α + β phase field, A varies between 30 and $70b^2$, and in the β phase field A varies between 300 and $700b^2$. The values of different parameters such as n, Q and A indicate operation of two different dislocation mechanisms in the α + β phase and β phase fields.

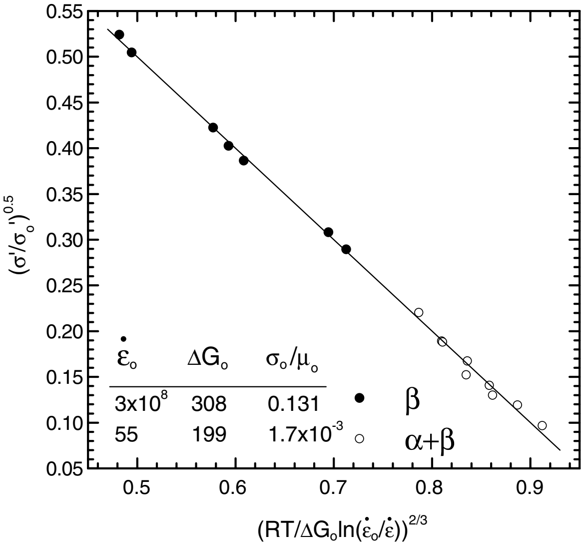

Fig. 9. Plot of normalized stress as function of temperature compensated strain rate for Zr–Nb–Sn in the α + β and β phase fields. The solid line is the theoretical relation as per Eq. (5). It is seen that using the appropriate constants $\dot{\varepsilon}_0$, ΔG_0 and σ'_0, the data set fits well with Eq. (5).

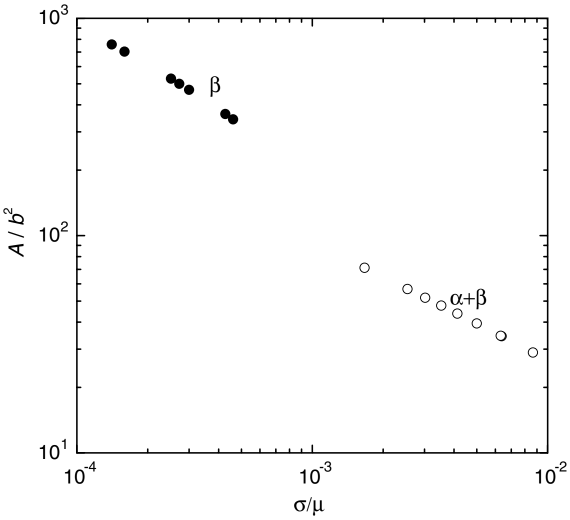

Fig. 10. Plots of normalized apparent activation area A vs. normalized stress, for both α + β and β phase fields.

4. Discussion

This investigation has found that Zr–Nb–Sn alloy when deformed in the temperature range 650–1050 °C exhibits three domains in the processing map where more than one deformation mechanisms are operative. On the basis of the nature of σ–ε behavior, deformed microstructure and associated strain rate sensitivity values (0.25), the domain occurring at 650 °C and at strain rates lower than $5 \times 10^{-3}\ \mathrm{s}^{-1}$ can be characterized by dynamic recovery. Dynamic recovery has been reported with similar characteristics under identical conditions of deformation in a CP Zr and Zircaloy-2 [5,8]. Since this domain is not well developed, a detailed characterization in terms of kinetic analysis was not possible.

The important observations in α + β phase field of D_2 domain are the following: relatively high strain rate sensitivity (≈0.3), reconstitution of the initial transformed β microstructure (consisting α′ plates) to an equiaxed α morphology, presence of substructure within equiaxed α grains and enhancement of hot ductility. These are indicative of the fact that the alloy is undergoing DRX in the α + β phase field. This is further supported by the linear plot of log(grain size) vs. log(Z) as shown in Fig. 11, which

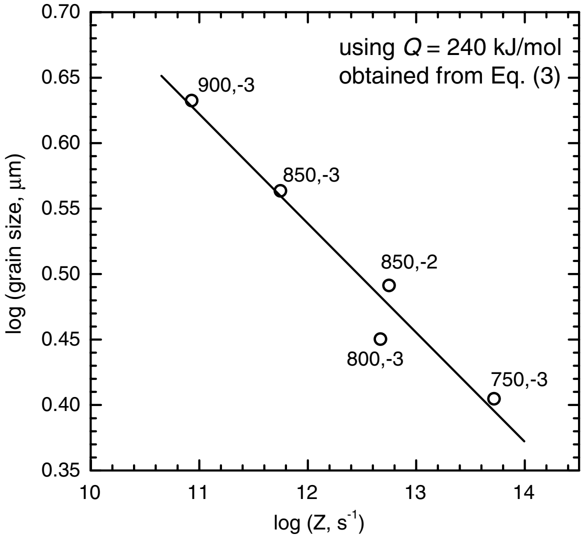

Fig. 11. Variation of log(grain size) vs. log(Z). The numbers indicated beside each data point represent the temperature in °C and log of strain rate in s^{-1}.

is considered to be one of the characteristic features of DRX [26]. Similar linear variations of log(grain size) with log(Z) have been reported during DRX in Ti [16,17] and Zr alloys [27]. In general, the values of n and Q are characteristic of a given rate controlling mechanism. From the estimated values of $n = 3.8$ and $Q = 259$ kJ/mol it is likely that a dislocation mechanism within the α grains may be involved in the process of DRX. An activation energy higher than the self diffusion and an activation area of the order of $50b^2$ rule out dislocation climb ($A \sim 1b^2$) and thermal breaking of attractive junctions as rate controlling mechanisms ($A \sim 10^2$ to 10^3b^2) [23,28], and suggests that mechanical recovery (cross-slip) of screw dislocations in α phase is involved in the process of DRX of Zr–Nb–Sn. In earlier studies too cross-slip has been found to be associated with the DRX process in Zr–2.5Nb [9] and Zircaloy-2 [27]. This conclusion is consistent with predictions of theoretical models of cross-slip as a thermally activated process [23,28].

In the high temperature ($T > 960$ °C) regime of domain D_2, the flow stresses are very low and independent of strain, the power dissipation efficiency is 40% (corresponding $m = 0.25$) and ductility is greater than 100%. Similar observations have been made during hot deformation of CP Zr [7] and Zr–2.5Nb alloy [18] in the β phase field, and it was concluded that these alloys undergo superplasticity at strain rates lower than 0.1 s^{-1}. The phenomenon of superplasticity in β phase is associated with the formation of fine subgrains within the large β grains and is explained by the sliding along these boundaries, commonly referred to as large-grain superplasticity (LGSP) [29,30]. In the present study $Q = 110$ kJ/mol, which is very close to that for self diffusion in β Zr (120 kJ/mol), suggests that the associated accommodation mechanism is likely to be diffusion controlled. However, $n = 4.2$ suggests the involvement of a dislocation mechanism. It may be noted that the computed activation area of $\sim 500b^2$ rules out climb as well as cross-slip as the accommodation mechanism. The underlying accommodation mechanism therefore appears to involve the non-conservative movement of jogs in which subgrain boundaries act as both sinks and sources for dislocations. Similar conclusions were drawn from an earlier study on the hot deformation behavior of Zr–2.5Nb in the β phase field [18].

The instability maps generated on the basis of the continuum instability criterion revealed that the alloy undergoes flow instability in both α + β phase field in the temperature range 650–850 °C and strain rates greater than 0.005 s^{-1}, and in β field at strain rates greater than 10 s^{-1}. The criterion was validated by microstructural examination of the specimen deformed in the instability regime. The manifestation of instability was in the form of flow localization, the severity of which reduced as the strain rate of deformation was lowered. These observations are consistent with features of instability recorded in various zirconium alloys [4–10].

A comparison of the hot deformation behavior of Zr–Nb–Sn alloy with other Zr alloys would be helpful in understanding the effect of major alloying additions. For this purpose, the processing maps of CP Zr, Zircaloy-2 (essentially binary alloy containing 1.5 Sn, an α stabilizer) and Zr–2.5Nb (Nb, a β stabilizer) are shown in Fig. 12. The details of optimum processing conditions, deformation mechanisms and description of deformed microstructures for these alloys have also been included for comparison in Table 2. The following important facts emerge on detailed comparison:

(i) For all the alloys of Zr studied, DRX of α is the prevalent mechanism during hot deformation in both single phase α (as in CP Zr and Zircaloy-2) and two phase α + β (as in binary Zr–2.5Nb and Zr–Nb–Sn alloys).
(ii) The optimum hot working conditions in the α (as in CP Zr and Zircaloy-2) and α + β phase

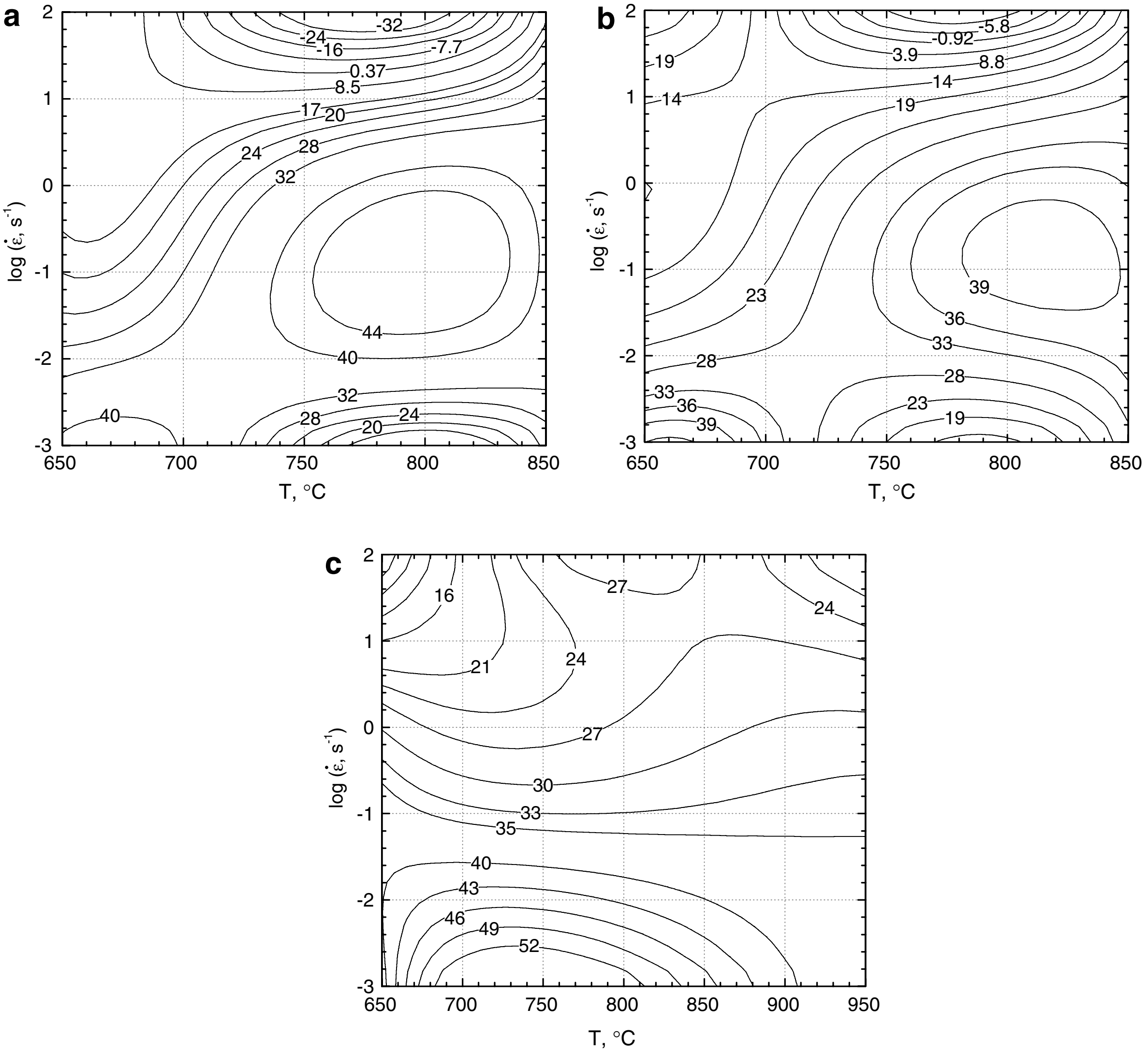

Fig. 12. Power dissipation efficiency maps at a strain of 0.5 showing various domains: (a) CP Zr (β-quenched) [5], (b) Zircaloy-2 (β-quenched) [8] and (c) Zr–2.5Nb (β-quenched) [9]. Contour numbers indicate efficiency of power dissipation in percent.

field (as in binary Zr–2.5Nb and Zr–Nb–Sn alloys) are associated with DRX for all the alloys of Zr.

(iii) The optimum hot working parameters (T and $\dot{\varepsilon}$) are unaltered by addition of Sn to CP Zr.

(iv) The strain rate for DRX is lowered by two orders of magnitude by Nb (as in Zr–2.5Nb and Zr–Nb–Sn) compared to CP Zr.

(v) The optimum strain rates for the hot working of Zr–2.5Nb and Zr–Nb–Sn alloys are identical although there is a slight increase in the corresponding temperature for the latter alloy.

(vi) Deformation characteristics of β phase field are not influenced significantly by alloying elements of different types (e.g. Sn, Nb).

(vii) Although there are some variations in the morphological details of deformed microstructures during DRX, a common feature is the presence of substructure in nearly equiaxed α grains in all the alloys.

(viii) The features of dynamic recovery of CP Zr, Zircaloy-2 and Zr–Nb–Sn alloys are similar.

It is clear from the preceding sections that Zr–Nb–Sn alloy exhibits three distinctly different

Table 2
Comparison of the hot deformation characteristics for various Zr alloys: optimum hot working parameters, deformed microstructure and deformation mechanisms

Alloy	Optimum hot working conditions		Deformation mechanism	Deformed microstructure	Reference
	T (°C)	$\dot{\varepsilon}$ (s^{-1})			
Zr (α)	800	10^{-1}	DRX of α	Equiaxed α grains with serrated boundaries, dislocation sub-structure within the equiaxed grains	[5,6]
Zircaloy-2 (α)	800	10^{-1}	DRX of α	Similar as α-Zr	[6,8]
Zr–2.5Nb (α + β)	750	10^{-3}	DRX leading to globularization of α phase	Nearly equiaxed α-grains separated by β phase film. Dislocation network within α-grains forming sub-boundaries	[9]
Zr–Nb–Sn (α + β)	900	10^{-3}	DRX of α phase	Equiaxed α grains with β phase at the triple junctions of grains, dislocation substructure within α-grains	This work
Zr (β)	1050	10^{-3}	Superplasticity	Deformed structure is masked by transformation	[7]
Zr–2.5Nb (β)	1100	10^{-3}	Superplasticity	Do	[18]
Zr–Nb–Sn (β)	1050	10^{-3}	Superplasticity	Do	This work

deformation mechanisms namely dynamic recovery, DRX and superplasticity depending on the temperature and strain rate of deformation. These three mechanisms are within the stable flow regime of the processing map and are expected to produce different microstructures thereby enabling microstructural control. It is also noted that both ductility and efficiency peak within the domain of DRX. The hot workability of Zr–Nb–Sn alloy may be optimized using processing maps by selecting the temperature–strain rate combination corresponding to the peak efficiency in the DRX domain, which is at 900 °C and 10^{-3} s^{-1}. Further the occurrence of microstructural instabilities as predicted by the continuum criterion given by Eq. (2) is validated by microstructural investigation. The condition of processing should be chosen such that the domain of microstructural instability is avoided. As regards the effect of alloying, it is seen that α-stabilizer such as Sn does not alter hot deformation characteristics of Zr in both α and β phase fields. While the DRX characteristics of α-Zr is strongly influenced by β stabilizer like Nb, the LGSP of β is not significantly altered. Since Sn does not have any effect on the hot deformation behavior of Zr, the deformation characteristics of Zr–Nb–Sn alloy resemble that of binary Zr–Nb alloy in α + β phase field.

5. Conclusion

On the basis of the processing map obtained for Zr–Nb–Sn alloy in the temperature range of 650–1050 °C and in the strain rate range 10^{-3}–10^{2} s^{-1}, detailed metallographic investigations and kinetic analysis performed, the following conclusions may be drawn:

1. Dynamic recrystallization of α phase in two phase α + β field occurs in the temperature range of 750–950 °C and strain rates lower than 10^{-2} s^{-1} with a peak efficiency of 43% at 910 °C and 10^{-3} s^{-1}.
2. The optimum processing parameters for hot working of Zr–Nb–Sn alloy in the α + β phase field are 910 °C and 10^{-3} s^{-1} at which dynamic recrystallization will result.
3. Zr–Nb–Sn alloy, when deformed at 650 °C and at rates lower than 10^{-2} s^{-1}, results in dynamic recovery, which is similar to that occurring in CP Zr and Zircaloy-2.
4. The alloy undergoes large-grain superplasticity in the β phase field at strain rates lower than 10^{-2} s^{-1}. The observed values of apparent activation energy (110 kJ/mol, nearly equal to self diffusion) and activation area ($\sim 500b^2$) suggest that underlying rate controlling accommodation mechanism is the non-conservative movement of jogs.
5. The material exhibits flow instabilities at lower temperatures (<850 °C) and at strain rates higher than 0.01 s^{-1} in the α + β range. In the β phase field, instabilities are predicted at $\dot{\varepsilon} > 10$ s^{-1}. Instabilities in α + β regime manifested in the form of localized flow. These deformation conditions must be avoided in processing the alloy.
6. The optimum hot working conditions are associated with DRX of α phase for all the alloys of Zr.

While β stabilizers like Nb has strong influence in lowering the strain rate for optimum DRX (compared to Zr), α stabilizer like Sn appears to have no influence on dynamic recrystallization. The hot deformation behavior of β phase is unaltered by alloying addition of either type.

Acknowledgements

Authors would like to acknowledge the experimental assistance received from Dr S.L. Wadekar, Materials Science Division, Bhabha Atomic Research Centre (BARC) and Shri. S. Sasidhar, Indian Institute of Science during the course of this work. Authors would like to thank Dr R. Tewari and Mr S. Neogy, Materials Science Division BARC for their help in transmission electron microscopy work.

References

[1] G. Sabol, G.R. Klip, M.G. Balfour, E. Roberts, Zirconium in the Nuclear Industry, in: Eighth International Symposium, ASTM STP 1023, 1989, p. 227.

[2] G.P. Sabol, G. Schoenberger, M.G. Balfour, IAEA Tech. Comm. Meeting on Materials for Advanced Water-Cooled Reactors, Plzen, Czech and Slovak Federal Republic, 14–17 May 1991, p. 50-1.

[3] A.V. Nikulina, in: Indo-Russian Conference on Nuclear Fuel fabrication, Hyderabad, India, 17–21 August 1998.

[4] A.V. Nikulina, V.A. Markelov, M.M. Peregud, V.N. Voevodin, V.L. Panchenko, G.P. Kobylyansky, J. Nucl. Mater. 238 (1996) 205.

[5] J.K. Chakravartty, Y.V.R.K. Prasad, M.K. Asundi, Metall. Trans. 22A (1991) 829.

[6] J.K. Chakravartty, Optimization of Hot Workability and Control of Microstructure in Zirconium Alloys, PhD thesis, Indian Institute of Science, Bangalore, 1992.

[7] J.K. Chakravartty, S. Banerjee, Y.V.R.K. Prasad, Scripta Metall. Mater. 26 (1992) 75.

[8] J.K. Chakravartty, S. Banerjee, Y.V.R.K. Prasad, M.K. Asundi, J. Nucl. Mater. 187 (1992) 260.

[9] J.K. Chakravartty, S. Banerjee, Y.V.R.K. Prasad, Mater. Sci. Technol. 12 (1996) 705.

[10] J.K. Chakravartty, G.K. Dey, S. Banerjee, Y.V.R.K. Prasad, J. Nucl. Mater. 218 (1995) 247.

[11] H.L. Gegel, J.C. Malas, S.M. Doraivelu, V.A. Shende, Metals Hand Book, vol. 14, American Society of Metals, Metals Park, OH, 1987, p. 417.

[12] Y.V.R.K. Prasad, T. Seshacharyulu, Int. Mater. Rev. 43 (1998) 243.

[13] Y.V.R.K. Prasad, S. Sasidhara, Hot Working Guide: A Compendium of Processing Maps, ASM International, Metals Park, OH, 1997.

[14] H. Ziegler, Progress in Solid Mechanics, vol. 4, Wiley, New York, 1963, p. 93.

[15] A.K.S. Kalyan Kumar, M.Sc. (Eng.) Thesis, Indian Institute of Science, Bangalore, India, 1987.

[16] T. Seshacharyulu, S.C. Medeiros, W.G. Frazier, Y.V.R.K. Prasad, Mater. Sci. Eng. A 284 (2000) 184.

[17] T. Seshacharyulu, S.C. Medeiros, W.G. Frazier, Y.V.R.K. Prasad, Mater. Sci. Eng. A 325 (2002) 112.

[18] R. Kapoor, J.K. Chakravartty, J. Nucl. Mater. 306 (2002) 126.

[19] V.V. Balasubrahmanyam, Y.V.R.K. Prasad, Mater. Sci. Technol. 17 (2001) 1222.

[20] V.V. Balasubrahmanyam, Y.V.R.K. Prasad, Mater. Sci. Eng. A 336 (2002) 150.

[21] H.E. Rosinger, A.E. Unger, Superplastic and strain rate dependent plastic flow of Zr–2.5Nb between 873 and 1373 K, AECL-6418, Atomic Energy Canada, Pinawa, Manitoba 1979.

[22] H. Conrad, J. Met. 16 (1964) 582.

[23] A.G. Evans, R.D. Rawlings, Phys. Status Solidi 34 (1969) 9.

[24] U.F. Kocks, A.S. Argon, M.F. Ashby, Prog. Mater. Sci. 19 (1975) 1.

[25] K. Ono, J. Appl. Phys. 39 (3) (1968) 1803.

[26] J.J. Jonas, G.M. Sellars, W.J.Mcg. Tegart, Met. Rev. 14 (1969) 1.

[27] J.K. Chakravartty, R. Kapoor, S. Banerjee, Z. Metallkd. 96 (2005) 645.

[28] E.A. Little, J. Aust. Inst. Met. 21 (1976) 50.

[29] P. Griffiths, C. Hammond, Acta Metall. 20 (1972) 935.

[30] T.G. Nieh, J. Wadsworth, Int. Mater. Rev. 44 (1999) 59.